J. Fluid Mech. (1998), *vol.* 368, *pp.* 1–26. Printed in the United Kingdom

Boundary layer receptivity to free-stream sound on parabolic bodies

By OSAMAH M. HADDAD† AND THOMAS C. CORKE

Illinois Institute of Technology, Fluid Dynamics Research Center, Chicago, IL 60616, USA

(Received 23 September 1996 and in revised form 4 September 1997)

We use a numerical approach to study the receptivity of the boundary layer flow over a slender body with a leading edge of finite radius of curvature to small streamwise velocity fluctuations of a given frequency. The body of interest is a parabola in order to exclude jumps in curvature, which are known sites of receptivity and which occur on elliptic leading edges matched to finite-thickness flat plates. The infinitesimally thin flat plate is the limiting solution for the parabola as the nose radius of curvature goes to zero. The formulation of the problem allows the two-dimensional unsteady Navier–Stokes equations in stream function and vorticity form to be converted to two steady systems of equations describing the basic (nonlinear) flow and the perturbation (linear) flow. The results for the basic flow are in excellent agreement with those in the literature. As expected, the perturbation flow was found to be a combination of an unsteady Stokes flow and Orr–Sommerfeld modes. To separate these, the unsteady Stokes flow was solved separately and subtracted from the total perturbation flow. We found agreement with the streamwise wavelengths and locations of Branches I and II of the linear stability neutral growth curve for Tollmien–Schlichting waves. The results showed an increase in the leading-edge receptivity with decreasing nose radius, with the maximum occurring for an infinitely sharp flat plate. The receptivity coefficient was also found to increase with angle of attack. These results were in qualitative agreement with the asymptotic analysis of Hammerton & Kerschen (1992). Good quantitative agreement was also found with the recent numerical results of Fuciarelli (1997), and the experimental results of Saric, Wei & Rasmussen (1994).

1. Introduction

The term 'receptivity' refers to the mechanism by which disturbances in the free stream, such as sound or vorticity, enter the boundary layer as small fluctuations of the basic state and excite unstable modes. These modes in the case of a Blasius boundary layer are of the Tollmien–Schlichting (T-S) type if the initial amplitudes of the disturbances are small. Although we understand well the process of linear and weakly nonlinear growth of T-S waves, practical applications aimed at predicting transition locations require accurately knowing their initial amplitudes. This is especially true for nonlinear interactions, such as with subharmonic resonance (see for example Corke & Mangano 1989), where there is an extremely sensitive (exponential) dependence of the amplitude of subharmonic three-dimensional modes on the initial amplitude of the fundamental T-S mode.

† Permanent address: Jordan University of Science and Technology, Mechanical Engineering Department, PO Box 3030, Irbid, Jordan.

Our understanding of the receptivity process has largely come from asymptotic theories. The earliest of these were by Goldstein (1983, 1985). These have set the theoretical framework, and especially emphasized the role of sharp changes in curvature as receptivity sites. One of the earliest physical experiments on leading-edge receptivity was for a sharp flat plate which was performed by Shapiro (1977). More recently, an elliptic leading edge joined to a flat plate was used in the experiments by Saric & Rasmussen (1992) and Saric, Wei & Rasmussen (1994). Lin, Reed & Saric (1990) performed a full Navier–Stokes (N-S) calculation to model those elliptic leading-edge experiments. Their numerical results were not complete in that it was difficult to distinguish between receptivity produced by the leading edge and that produced locally at the joint between the ellipse and flat plate. That geometry also makes it difficult to separate the effects of curvature and pressure gradient on receptivity. The later work by Lin, Reed & Saric (1992) addressed the aspect of the joint by using large-aspect-ratio super-ellipses.

The parabolic geometry has the advantage of constant curvature. Also, for a zero angle of attack, the pressure gradient is everywhere favourable. These make the parabolic body well suited to isolate the leading-edge receptivity mechanism from other mechanisms or sites of receptivity (although from a practical standpoint, to be used in a wind tunnel, the parabolic body would eventually need to be faired to a flat plate at a downstream location). Murdock (1980, 1981) used a numerical approach to study the receptivity over an infinitely thin flat plate and parabolic cylinders. For both cases, he modelled the receptivity through a parabolized form of the unsteady N-S equations. More recently, Hammerton & Kerschen (1992) used asymptotic analysis to study the effect of the nose radius of curvature on receptivity of the boundary layer over a parabolic leading edge subject to acoustic excitation. In that study, the nose radius entered the theory through a Strouhal number based on the frequency of the sound and the free-stream velocity, and using the nose radius as the characteristic length. Their results showed a strong dependence of receptivity on the Strouhal number. Up to now, there have been no other analytical solutions or physical experiments which have dealt with parabolic leading edges.

Our objective was to perform a numerical simulation of the flow over a parabolic leading edge in a uniform flow with a small-amplitude acoustic disturbance. The previous cited numerical work solved the nonlinear time-dependent N-S equations. The experimental evidence is that the process of receptivity to these disturbances is linear, and the resulting growth of instabilities is spatial. Therefore, we will develop a more efficient spatial formulation in which the basic and unsteady flows will be decoupled, and solved separately.

2. The physical problem

We consider the two-dimensional laminar incompressible flow of a constant-property fluid over a parabolic body such as is schematically represented in figure 1. The equation of the surface of the parabolic body is given by

$$x(y) = \frac{1}{2R}(y^2 - R^2). \tag{1}$$

The radius of curvature $r(x)$ of the parabola $x(y)$ is given by

$$r(x) = \frac{(1 + x'^2)^{3/2}}{x''} = \left[\frac{8(R + x)^3}{R}\right]^{1/2}. \tag{2}$$

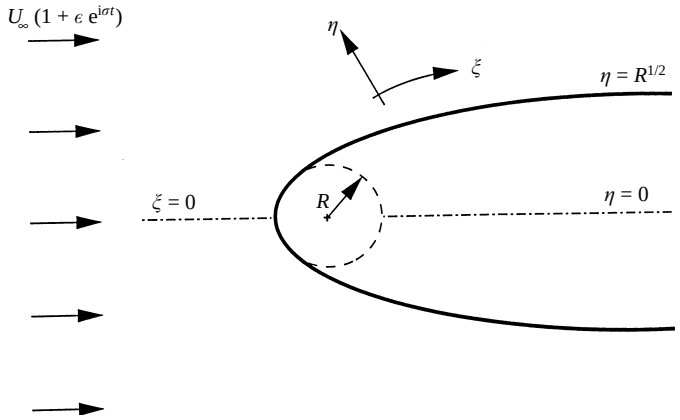

FIGURE 1. Schematic of parabolic body in a symmetric mean flow with a superposed small free-stream oscillation.

By applying (2) at the leading edge ($y = 0$ and $x = -R/2$) we obtain $r = R$, and thus R is recognized to be the nose radius of curvature of the parabola. Note that R in its dimensional form is the nose radius of curvature, but when non-dimensionalized, it is Reynolds number based on the nose radius of curvature, *Re*.

3. Governing equations and boundary conditions

3.1. *Governing equations*

We consider the full N-S equations to study the receptivity of the boundary layer because the parallel flow assumption (which leads to the Orr–Somerfeld (O-S) equation) precludes the transfer of energy from the long-wavelength acoustic disturbance to the short-wavelength T-S wave. In the Cartesian coordinate system (x, y), the non-dimensional N-S equations in stream function (ψ) and vorticity (ω) variables are given in the form

$$\psi_{xx} + \psi_{yy} = -\omega, \tag{3}$$

$$\omega_t + \psi_y \omega_x - \psi_x \omega_y = \omega_{xx} + \omega_{yy}, \tag{4}$$

where subscripts denote partial differentiation. In non-dimensionalizing the variables, the following dimensionless group of variables were introduced:

$$x = \frac{x^*}{\nu/U_\infty}, \quad y = \frac{y^*}{\nu/U_\infty}, \quad t = \frac{t^*}{\nu/U_\infty^2}, \quad \omega = \frac{\omega^*}{U_\infty^2/\nu}, \quad \psi = \frac{\psi^*}{\nu}. \tag{5}$$

The geometry of the body suggests that the problem be formulated in terms of parabolic coordinates. The dimensionless parabolic coordinates (ξ, η) are related to the dimensionless Cartesian coordinates (x, y) by

$$x = \frac{\xi^2 - \eta^2}{2}, \qquad y = \xi\eta. \tag{6}$$

Note here that the body surface is located at $\eta = R^{1/2}$. Based on equation (6), equations (3) and (4) can be rewritten in parabolic coordinates as

$$\psi_{\xi\xi} + \psi_{\eta\eta} = -\left(\xi^2 + \eta^2\right)\omega, \tag{7}$$

$$\left[\frac{\partial^2}{\partial\xi^2}+\frac{\partial^2}{\partial\eta^2}+\frac{\partial\psi}{\partial\xi}\frac{\partial}{\partial\eta}-\frac{\partial\psi}{\partial\eta}\frac{\partial}{\partial\xi}-\left(\xi^2+\eta^2\right)\frac{\partial}{\partial t}\right]\omega=0. \tag{8}$$

In order to remove the singularity in vorticity at the leading edge for the limiting case of an infinitely thin flat plate, we followed Davis (1972) and introduced the new variables f and g which are related to ψ and ω by

$$\psi=\xi f(\xi,\eta,t), \qquad \omega=-\frac{\xi}{\left(\xi^2+\eta^2\right)}g(\xi,\eta,t). \tag{9}$$

With the new dependent variables given by (9) the governing equations (7) and (8) become

$$f_{\eta\eta}-g+f_{\xi\xi}+\frac{2}{\xi}f_\xi=0, \tag{10}$$

$$g_{\eta\eta}+\left(f+\xi f_\xi-\frac{4\eta}{\xi^2+\eta^2}\right)g_\eta+\left(\frac{\xi^2-\eta^2}{\xi^2+\eta^2}f_\eta-\frac{2\eta}{\xi^2+\eta^2}\left(f+\xi f_\xi\right)\right)g$$
$$-\xi g_\xi\left(f_\eta+\frac{4}{\xi^2+\eta^2}\right)-\left(\xi^2+\eta^2\right)g_t+g_{\xi\xi}+\frac{2}{\xi}g_\xi=0. \tag{11}$$

We note that these equations are parabolic in ξ when the last two terms in both equations are neglected. This fact had been exploited by Davis (1972) to formulate an efficient numerical method.

3.2. *Boundary conditions*

At the wall, the no-slip, no-penetration conditions are satisfied by

$$f(\xi,R^{1/2})=0 \quad \text{and} \quad f_\eta(\xi,R^{1/2})=0. \tag{12}$$

The vorticity at the wall is obtained by applying the stream function equation (7) at the wall where $\psi_\xi=\psi_{\xi\xi}=\psi_\eta=0$, giving

$$g(\xi,R^{1/2})=f_{\eta\eta}. \tag{13}$$

At the free-stream, the flow is uniform giving

$$f_\eta\to 1 \quad \text{as} \quad \eta\to\infty. \tag{14}$$

The free-stream is also vortex free, so that

$$g\to 0 \quad \text{as} \quad \eta\to\infty. \tag{15}$$

4. Perturbation of the governing equations and boundary conditions

To investigate the receptivity to an acoustic wave, we considered the free stream to be composed of a uniform flow in the x-direction with a superposed uniform small oscillation of frequency σ and amplitude ϵ, namely

$$\psi_\infty=\left(1+\epsilon\,\mathrm{e}^{\mathrm{i}\sigma t}\right)\xi\eta, \tag{16}$$

where ϵ is sufficiently small for linearization. We decomposed the unsteady flow field into a steady basic state plus an unsteady perturbation (in normal-mode form), according to

$$f(\xi,\eta,t)=F(\xi,\eta)+\epsilon\,\mathrm{e}^{\mathrm{i}\sigma t}\tilde{f}(\xi,\eta), \tag{17}$$

$$g(\xi,\eta,t) = G(\xi,\eta) + \epsilon\, \mathrm{e}^{\mathrm{i}\sigma t}\tilde{g}(\xi,\eta). \tag{18}$$

Substituting these equations back into the governing equations and boundary conditions, and equating terms of equal powers of ϵ leads to the governing equations for the basic and perturbation flow fields.

The basic flow (zero-order terms in ϵ) is governed by the following set of differential equations:

$$F_{\eta\eta} - G + F_{\xi\xi} + \frac{2}{\xi}F_{\xi} = 0, \tag{19}$$

$$G_{\eta\eta} + \left[F + \xi F_{\xi} - \frac{4\eta}{\xi^2+\eta^2}\right]G_{\eta} + \left[\frac{\xi^2-\eta^2}{\xi^2+\eta^2}F_{\eta} - \frac{2\eta}{\xi^2+\eta^2}F - \frac{2\xi\eta}{\xi^2+\eta^2}F_{\xi}\right]G - \left[\xi F_{\eta} + \frac{4\xi}{\xi^2+\eta^2}\right]G_{\xi} + G_{\xi\xi} + \frac{2}{\xi}G_{\xi} = 0 \tag{20}$$

with boundary conditions

$$F = 0, \quad F_{\eta} = 0 \quad \text{and} \quad G = F_{\eta\eta} \quad \text{at} \quad \eta = R^{1/2}, \tag{21}$$

$$F_{\eta} \to 1 \quad \text{and} \quad G \to 0 \quad \text{as} \quad \eta \to \infty. \tag{22}$$

These equations governing the basic flow are steady, coupled and nonlinear in the real variables F and G.

After linearizing in ϵ, the perturbation flow is governed by

$$\tilde{f}_{\eta\eta} - \tilde{g} + \tilde{f}_{\xi\xi} + \frac{2}{\xi}\tilde{f}_{\xi} = 0, \tag{23}$$

$$\tilde{g}_{\eta\eta} + \left[F + \xi F_{\xi} - \frac{4\eta}{\xi^2+\eta^2}\right]\tilde{g}_{\eta} - \left[\xi F_{\eta} + \frac{4\xi}{\xi^2+\eta^2}\right]\tilde{g}_{\xi} + \left[\frac{\xi^2-\eta^2}{\xi^2+\eta^2}F_{\eta} - \frac{2\eta}{\xi^2+\eta^2}F\frac{2\xi\eta}{\xi^2+\eta^2}F_{\xi}\right]\tilde{g} + \left[\frac{\xi^2-\eta^2}{\xi^2+\eta^2}G - \xi G_{\xi}\right]\tilde{f}_{\eta} + \left[\xi G_{\eta} - \frac{2\xi\eta}{\xi^2+\eta^2}G\right]\tilde{f}_{\xi} + \left[G_{\eta} - \frac{2\eta}{\xi^2+\eta^2}G\right]\tilde{f} - \mathrm{i}\sigma\left(\xi^2+\eta^2\right)\tilde{g} + \tilde{g}_{\xi\xi} + \frac{2}{\xi}\tilde{g}_{\xi} = 0 \tag{24}$$

with boundary conditions

$$\tilde{f} = 0, \quad \tilde{f}_{\eta} = 0 \quad \text{and} \quad \tilde{g} = \tilde{f}_{\eta\eta} \quad \text{at} \quad \eta = R^{1/2}, \tag{25}$$

$$\tilde{f}_{\eta} \to 1 \quad \text{and} \quad \tilde{g} \to 0 \quad \text{as} \quad \eta \to \infty. \tag{26}$$

These equations are steady, coupled and linear in the complex variables $\tilde{f}$ and $\tilde{g}$. The disturbance frequency, σ, appears explicitly in them. It is important to point out that these two sets of equations were first obtained by Herbert (1991).

5. Numerical formulation

5.1. *Grid generation and computational domain*

Among the advantages of using parabolic coordinates is that it allowed us to reduce any spurious receptivity that might have been produced by non-uniformities (discrete steps) in the body contour or the numerical grid. The non-dimensional length of the body, measured from the leading edge along the chord, was $\xi_{max} = 3.5 \times 10^5$. In the wall-normal direction, the free stream is considered to be at $\eta_{max} = 35$, measured from

the surface of the parabola. This was equivalent to ten times the maximum boundary layer thickness.

The number of points in the computational grid was determined while monitoring the solution for the mean flow. For example, the asymptotic solution was known to be Blasius (Davis 1972), and far from the leading edge, Davis had used the Blasius solution as his outflow boundary condition. In the end we used 500 grid points in the streamwise direction on each side of the body (i.e. upper and lower sides). We did not exploit symmetry of the flow since we also studied cases with non-zero angles of attack. In the wall-normal direction, 36 grid points were used. In regions of large gradients near the leading edge and wall, the grid points were more closely spaced. Robert's stretching transformation (Anderson, Tannehill & Pletcher 1984) was used for that purpose.

Although the grid was essentially determined on the basis of the mean flow calculations, we were careful that there were always at least ten numerical points per T-S wavelength in the streamwise direction.

5.2. *Finite difference scheme*

The governing equations for both the basic and perturbation flows were solved on the same numerical grid using a finite difference approach. Central differencing was used whenever possible, otherwise forward or backward differencing was used as applicable. The finite difference scheme was second-order accurate throughout the grid.

For numerical simulations of the spatially evolving laminar–turbulent transition process in boundary layers using the complete N-S equations, the treatment of the outflow boundary requires special attention. The disturbances must pass through this boundary without causing reflections that would significantly alter the flow upstream. This was achieved most efficiently by suppressing the elliptic terms (the last two terms in equations (19) and (20), and (23) and (24)) in each of the governing equations at the outflow boundary using a buffer domain (Kloker, Konelmann & Fasel 1993). The parabolizing of the governing equations in the outflow buffer zone was first introduced by Streett & Macaraeg (1989). Since then, this approach has been extensively used by many investigators, for example: Joslin & Streett (1992) and Kloker *et al.* (1993).

To implement the non-reflecting boundary condition at the outflow, a buffer zone was specified in which the elliptic terms in the governing equations were multiplied by a weighting factor, s. The weighting factor was a function of streamwise location only. At the begining of the buffer zone, $s = 1$; at the end, which corresponds to the outflow boundary, $s = 0$. In order to smoothly transition from 1 to 0, a multiplicative weighting factor of the following form was used:

$$s(i) = \frac{1 + \tanh(arg)}{2}, \tag{27}$$

where

$$arg = 4\left\{1 - \frac{2(i - i_{buf})}{(I_{max} - i_{buf})}\right\}. \tag{28}$$

Here, i is the numerical index in the streamwise direction, i_{buf} is the index i at the begining of the buffer zone, and I_{max} is the maximum value of i. The length of the buffer zone is an important parameter. In our case it was set to be equivalent to approximately four times the expected T-S wavelength, λ_{TS}. Joslin & Streett (1992) recommended a length equivalent to at least $3\lambda_{TS}$ so that our choice was conservative.

5.3. *Method of solution*

The nonlinear basic-flow equations were formulated into a linear set using Newton's linearization technique. The resulting system of linear algebraic equations for the basic flow, as well as the perturbation equations were solved using a standard banded matrix solver. All calculations were done in double precision arithmetic. For most of the nose Reynolds number (Re) cases considered here, the basic-flow code required six or seven iterations to converge.

Our method of formulation lead to a decoupling of the basic flow and perturbation equations. Thus the two systems of equations were solved separately. The basic flow variables, F and G, which appear in the metrics of the perturbation equations, are determined beforehand for a given Reynolds number. Conditions for different acoustic frequencies, σ, did not require a recalculation of the basic flow. For further details on the method of solution, the reader is referred to Haddad (1995).

6. Numerical results

An example of the sensitivity of the numerical results to the number of computational grid points is shown in figure 2. This shows the wall vorticity for different computational grid sizes for $Re = 10$. The basic flow over the parabolic body is known to approach Blasius flow far downstream. This leads the vorticity at the wall to become invariant in the flow direction away from the leading edge. The results in figure 2 for two cases with grid sizes of 500×27 (dotted line) and 500×30 (dashed line) show a trend far downstream which is clearly wrong. The other cases shown in the figure, with a larger number of wall-normal grid points, all collapse on a single curve. These show the proper downstream asymptote which agrees with a Blasius flow. The solid curve which corresponds to the grid size of 500×36 was used throughout this study.

6.1. *Basic flow*

In order to validate our results for the basic flow, the surface pressure and skin friction distributions were determined for different nose Reynolds numbers and compared with corresponding ones obtained by Davis (1972). From the x-momentum equation, the surface pressure is given by

$$\frac{\partial p}{\partial x} = -\frac{\partial \omega}{\partial y}. \tag{29}$$

Equation (29) can be rewritten in parabolic coordinates as

$$\frac{\partial p}{\partial \xi} = \frac{\xi}{\xi^2 + \eta^2}\left[\frac{\partial g}{\partial \eta} - \frac{2\eta}{\xi^2 + \eta^2} g\right]. \tag{30}$$

To remove the singularity in the pressure at the leading edge for the case of an infinitely thin body, we follow Davis (1972) and introduce

$$P = p - \frac{\eta}{\xi^2 + \eta^2} g(0, R^{1/2}). \tag{31}$$

The streamwise pressure gradient along the surface of the parabola is then given by

$$\frac{\partial P}{\partial \xi} = \frac{\xi}{\xi^2 + \eta^2}\left[\frac{\partial g}{\partial \eta} - \frac{2\eta}{\xi^2 + \eta^2}(g - g_o)\right], \tag{32}$$

where $g_o = g(0, R^{1/2})$. Using the pressure at downstream infinity on the lower surface as a reference pressure, the surface pressure was found by integrating (trapezoidal)

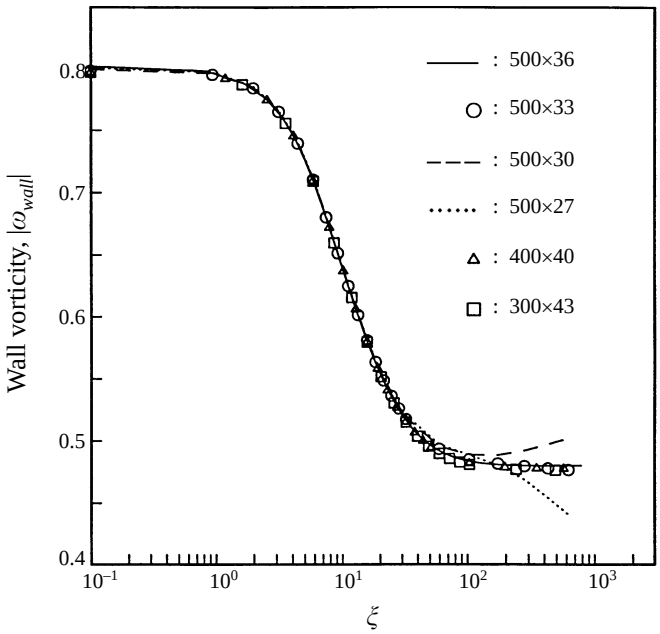

FIGURE 2. Effect of computational grid size on the vorticity along the surface of a parabolic cylinder; $Re = 10$.

from downstream infinity back along the surface. The pressure distributions for different nose Reynolds numbers from 0 (infinitely sharp flat plate) to 1000 are shown in figure 3(*a*). The symbols correspond to the results from Davis (1972). The agreement is very good. Our results are expected to be more accurate than Davis's since his formulation was only first-order accurate.

In terms of the pressure distribution, we observe that for these cases with zero angle of attack, the pressure gradient is everywhere favourable. The downstream distance where the pressure distribution asymptotes into the Blasius distribution is further as the nose radius Reynolds number increases. We chose to use the parabolic coordinate in the flow direction, ξ, on a log scale in order to magnify the region close to the leading edge. In reality, the distance to the Blasius asymptote is relatively close to the leading edge. For example for $Re = 10$ the asymptote is at $\xi \simeq 60$ where $Re_x \simeq 2000$ ($Re_x^{1/2} \simeq 45$).

Another fundamental result for the basic flow is the skin friction distribution. The skin friction coefficient is defined as

$$C_f = \frac{\tau_w^*}{\rho U_\infty^2}, \tag{33}$$

where $\tau_w^* = \mu(\partial u^*/\partial y^*)|_w$. In parabolic coordinates, the skin friction coefficient is given by

$$C_f = \frac{\xi}{\xi^2 + \eta^2} g(\xi, R^{1/2}). \tag{34}$$

Scaled skin friction distributions for different nose Reynolds numbers are shown in figure 3(*b*). Again we have excellent agreement with the results of Davis (1972), which are shown as symbols in the figure. These distributions look qualitatively like the pressure distributions, with a maximum at the leading edge which grows larger as the

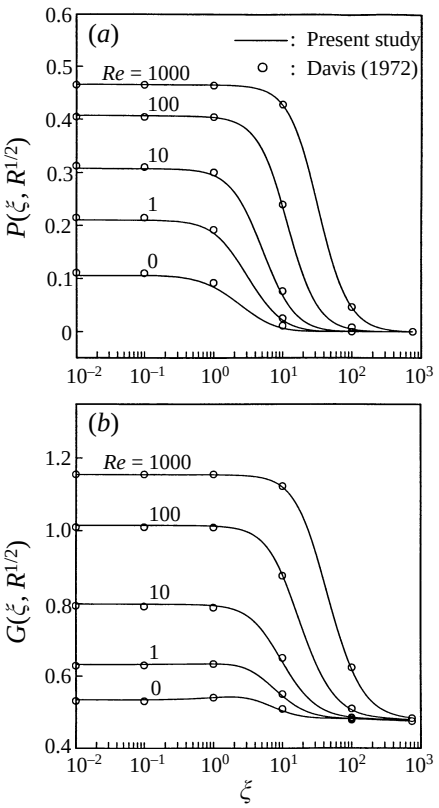

FIGURE 3. (*a*) Surface pressure and (*b*) skin friction distributions on parabolic bodies with different nose Reynolds numbers.

nose Reynolds number increases. Further downstream all the distributions asymptote to the Blasius value.

Mean velocity profiles at different downstream locations for an intermediate Reynolds number of 10 are shown in figure 4(*a*). Shown above each profile are the corresponding Re_x values. Close to the leading edge, we observe a slight overshoot in the mean velocity near the wall. This is attributed to the localized accelerating stagnation point flow (Hiemenz flow) that ocurs near the leading edge. In the analysis of Hammerton & Kerschen (1992), a Hiemenz profile was used as an initial condition at the leading edge. The profiles in figure 4(*a*) gradually approach the Blasius profile as we move downstream away from the leading edge. This is documented in figure 4(*b*), where we compare one of the mean profiles with the Blasius profile.

6.2. *Perturbation field*

The remaining figures deal with the solution of the perturbation flow which is governed by equations (23) and (24) with boundary conditions given in equations (25) and (26). For most of these results, a dimensionless free-stream oscillation frequency of $\sigma = 2\pi f \nu / U_\infty^2 = 230 \times 10^{-6}$ was used. This frequency crosses the upper tip of the neutral curve for the linear growth of disturbances in a Blasius layer. This higher frequency was chosen so that we could easily reach the location of the second neutral branch (II) within our computational domain. This was important in order to supply an additional check on the T-S instability that emerges in our calculations.

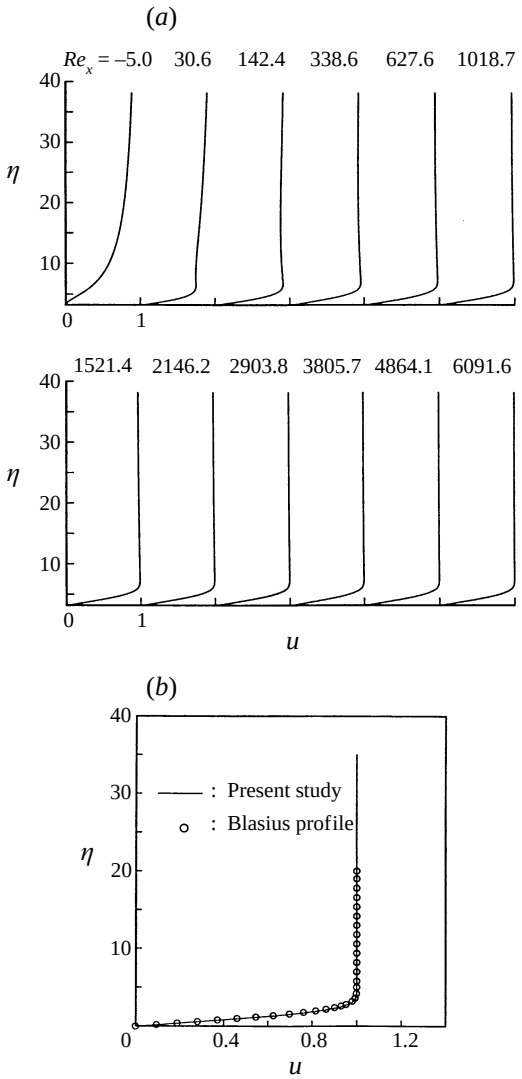

FIGURE 4. (*a*) Basic flow streamwise velocity profiles at consecutive downstream locations near the leading edge, and (*b*) comparison of profile at $Re_x = 82,286$ to Blasius; $Re = 10$.

A further motivation was that this frequency was primarily used in the numerical simulations of Lin *et al.* (1990, 1992). The lower frequency at $F = 56 \times 10^{-6}$ was also investigated in order to compare to Murdock (1981). This is contained in Haddad's (1995) thesis.

The first cases we present are for an infinitely thin flat plate ($Re = 0$). This allowed us to compare some of our results to previous analytic results by Ackerberg & Phillips (1972). Figure 5 shows the magnitude of the perturbation wall vorticity versus the dimensionless distance along the chord, Re_x, for $Re = 0$. Figure 5(*a*) has been scaled to show the large peak in the vortivity at the leading edge. Figure 5(*b*) is a magnified view which shows the spatial oscillations in the vorticity that occur downstream of the leading edge. We associate these oscillations with instability waves which are excited by the free-stream oscillations. For reference on this figure, we have indicated a scale

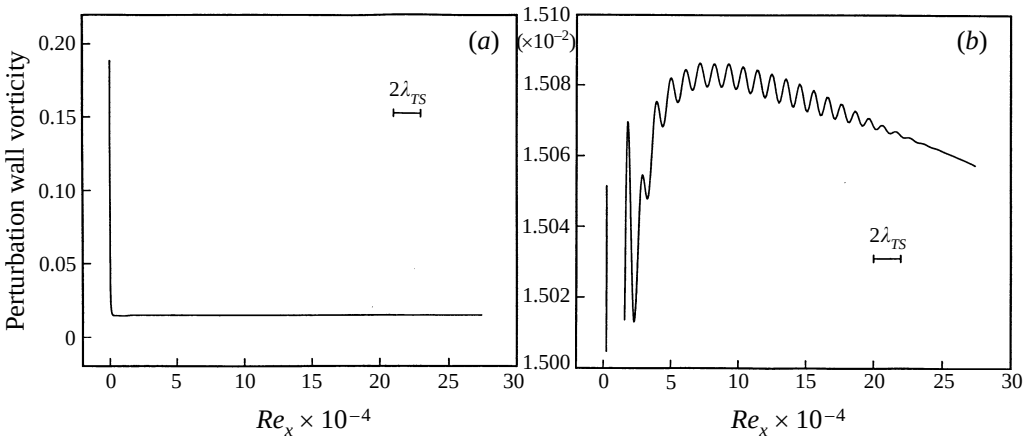

FIGURE 5. (*a*) Perturbation wall vorticity along the surface of a parabola with scale to encompass the peak at the leading edge, and (*b*) with a magnified scale to show fluctuations further downstream; $Re = 0$.

which corresponds to two T-S wavelengths. The wavelength of oscillations in the wall vorticity appears to match this quite well. Further evidence of T-S growth will come from subsequent figures.

The wall-normal distributions of the streamwise perturbation velocity amplitude at different x-locations along the surface of the flat plate are shown in figure 6. The corresponding Re_x values are shown above each profile. These distributions show a peak away from the wall which grows in amplitude up to a certain distance from the leading edge, and then decays further downstream.

Ackerberg & Phillips (1972) presented asymptotic as well as numerical solutions of the unsteady boundary-layer equations for the incompressible flow over a flat plate subject to small fluctuations in the free-stream velocity. Owing to the use of non-similar variables, both our profiles and theirs are dependent on the streamwise coordinate. In order to compare our results, we chose profiles at representative streamwise locations. From Ackerberg & Phillips, we picked the profile at $x = 4.0$. We compared this to our profile at $Re_x = 17\,795$. The comparison is shown in figure 7 in terms of the real and imaginary parts of the streamwise perturbation velocity, u'. Here we observe excellent agreement between our results.

In the remaining figures we primarily focus on an intermediate-thickness parabola with a nose Reynolds number of 10. Figure 8 shows the magnitude of the perturbation wall vorticity along the parabolic surface for this case. This is equivalent to figure 5 which was for $Re = 0$. As before, part (*a*) of the figure is scaled to show the peak in the vorticity that occurs at the leading edge; part (*b*) of the figure shows a magnified view which is intended to show the spatial oscillations in the vorticity at the wall that occur further downstream.

As with the $Re = 0$ case, the magnified view of the perturbation wall vorticity shows spatial oscillations with a wavelength that closely matches the expected T-S wavelength. These oscillations appear to start right at the leading edge. The vorticity fluctuations produced at the leading edge are convected in the flow direction and eventually are expected to include T-S waves. At our excitation frequency, the amplified region for T-S waves falls in the range $70\,000 \leqslant Re_x \leqslant 145\,000$. Outside this region, T-S waves are expected to decay.

The wall-normal distributions of the streamwise perturbation velocity amplitude at

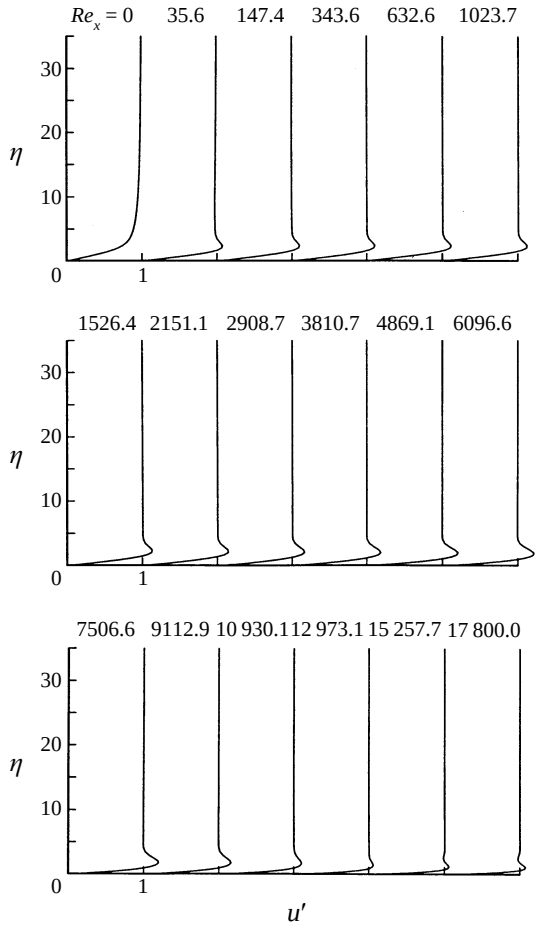

FIGURE 6. Wall-normal profiles of streamwise perturbation velocity amplitude at consecutive downstream locations before subtracting the Stokes wave; $Re = 0$.

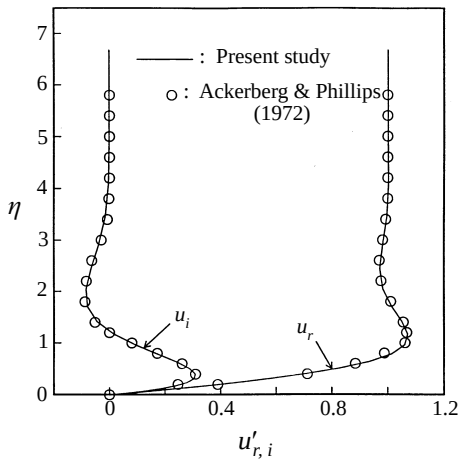

FIGURE 7. Comparison of real and imaginary parts of the streamwise perturbation velocity to that of Ackerberg & Phillips (1972); $Re = 0$.

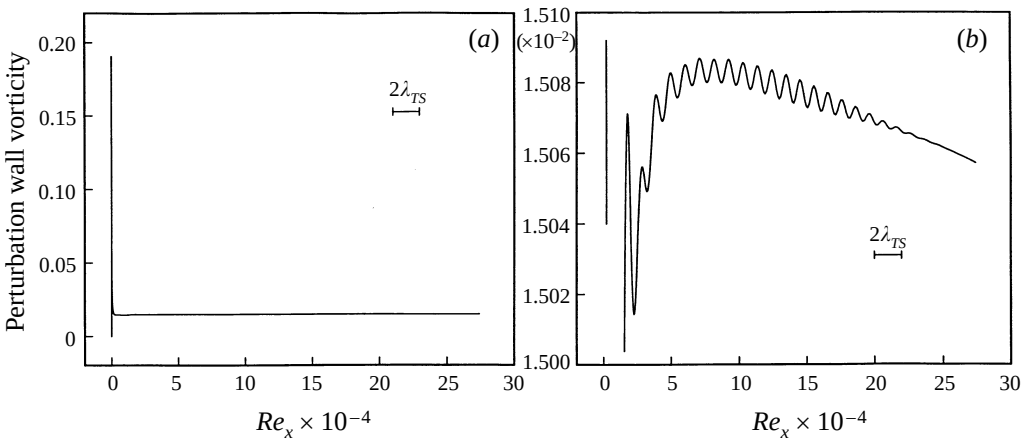

FIGURE 8. (*a*) Perturbation wall vorticity along the surface of parabola with scale to encompass the peak at the leading edge and (*b*) with a magnified scale to show fluctuations further downstream; $Re = 10$.

different streamwise stations along the surface of the body are shown in figure 9. The corresponding Re_x values are shown above each profile. These profiles are directly comparable to those in figure 6 which were for $Re = 0$.

In both Reynolds number cases, the perturbations are expected to be a combination of a Stokes wave and a T-S wave. The goal of this work was to determine the amplitude of the T-S waves that were excited by the free-stream oscillations. Therefore we needed to subtract the component of the perturbation velocity field which was due to the Stokes wave. To achieve this, the unsteady Stokes flow was computed separately on the same computational grid and subtracted from the total perturbation flow. The result would then leave only the component due to T-S waves. The determination of the Stokes-wave amplitude distribution is presented in the next subsection.

6.3. *Stokes wave*

The Stokes-wave solution due to an oscillating flat plate or free stream is an exact solution of the N-S equations which can be found in any standard textbook on viscous flows (e.g. Panton 1984). Our interest is in parabolic bodies and therefore we developed a numerical solution for a Stokes wave over parabolic bodies produced by a periodic free-stream oscillation. The limiting case of $Re = 0$ provided a convenient check of our approach and of the accuracy of the solution.

To obtain the governing equations for the Stokes flow, we started with equations (3) and (4), less the convective-inertia terms:

$$\psi_{xx} + \psi_{yy} = -\omega, \tag{35}$$

$$\omega_t = \omega_{xx} + \omega_{yy}. \tag{36}$$

These are subject to the same boundary conditions which were described earlier in §§ 3 and 5. Following the same procedures described in §§ 4 and 5, the governing equations were converted to parabolic coordinates and then transformed to remove the singularity at the leading edge in vorticity for the infinitely thin flat plate ($Re = 0$). We then introduced the normal-mode form which was given in equations (17) and

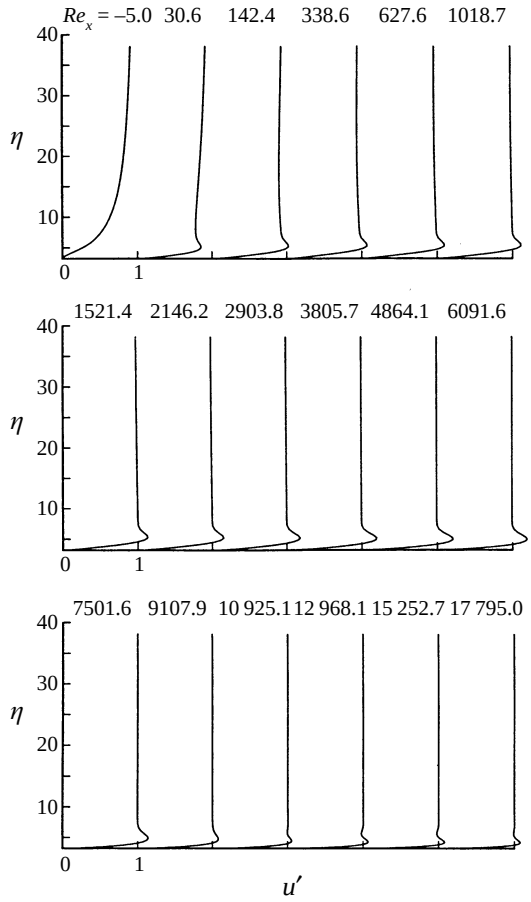

FIGURE 9. Wall-normal profiles of streamwise perturbation velocity amplitude at consecutive downstream locations before subtracting the Stokes wave; $Re = 10$.

(18) to obtain the perturbation equations:

$$\tilde{f_{\eta\eta}} - \tilde{g} + \tilde{f_{\xi\xi}} + \frac{2}{\xi}\tilde{f_{\xi}} = 0, \tag{37}$$

$$\tilde{g_{\eta\eta}} - \frac{4\eta}{\xi^2+\eta^2}\tilde{g_{\eta}} - \frac{4\xi}{\xi^2+\eta^2}\tilde{g_{\xi}} - \mathrm{i}\sigma\left(\xi^2+\eta^2\right)\tilde{g} + \tilde{g_{\xi\xi}} + \frac{2}{\xi}\tilde{g_{\xi}} = 0. \tag{38}$$

We note that eliminating the convective-inertia terms removed any influence of the basic flow variables on the perturbation field.

The equations for the Stokes flow were discretized on the same numerical grid used for the other calculations. We used the same approach and finite difference schemes described previously in § 5.

In order to check the solution, we first examined the case with $Re = 0$ (flat plate) for which an analytic solution exists. A sample of the results is given in figure 10, which shows wall-normal distributions of the streamwise velocity fluctuation amplitude at consecutive downstream locations. The analytic solution is valid for an infinitely long flat plate, without a leading edge. To validate our results, two arbitrary profiles at two different downstream locations, away from the leading edge ($Re_x = 27\,141$ and

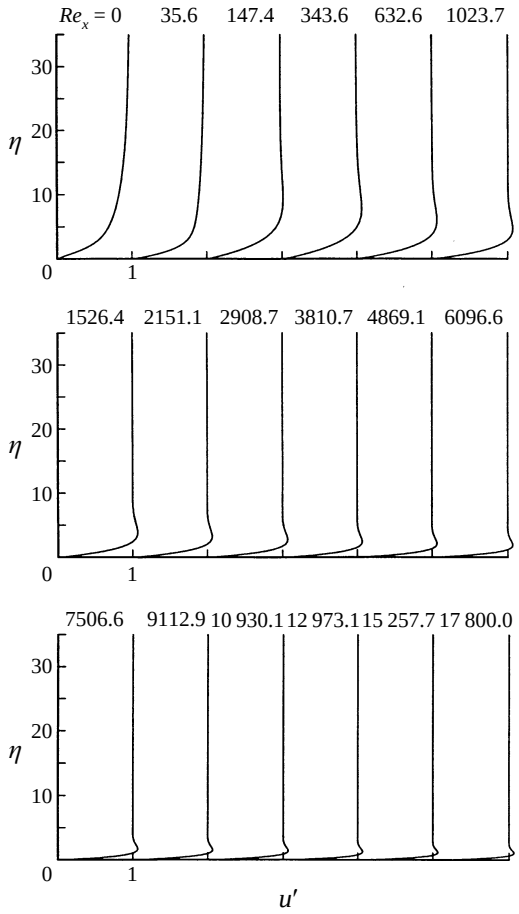

FIGURE 10. Stokes-wave wall-normal profiles of streamwise perturbation velocity amplitude at consecutive downstream locations; $Re = 0$.

187 427), were selected. Here we were interested in verifying the streamwise similarity of our solution, as well as comparing it to the analytic result. The comparison of these two profiles to the analytic solution is shown in figure 11. Here the numerical solution is shown by the symbols. These collapse onto a single profile which is the analytic solution (solid curve). This result substantiates our solution and provided confidence for considering cases of different nose Reynolds numbers.

We reiterate that the purpose of obtaining the Stokes-wave profiles was to separate out the component in the perturbation velocity field due to the Stokes wave in order to leave only the component due to the T-S waves. The method for removing the Stokes wave was to simply perform a point-by-point subtraction of the Stokes solution from the total (Stokes plus T-S) perturbation solution. Since both the total perturbation and Stokes flows are complex, the real amplitude was first computed for both before a point-by-point subtraction was performed. This was done for each nose Reynolds number case. The results of this process are presented in the following subsection.

6.4. *Receptivity results*

In this subsection we now focus on determining the amplitude of T-S waves which result from the small-amplitude free-stream oscillation. Here, the contribution of the

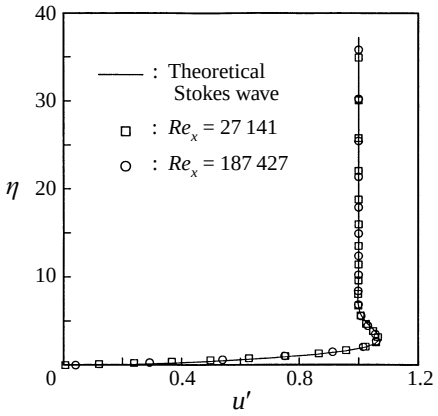

FIGURE 11. Comparison of computed amplitude profiles for Stokes wave to theoretical profile; $Re = 0$.

Stokes flow to the perturbation flow will be subtracted. As before, we use the $Re = 0$ and 10 cases to highlight the results. These will then be combined with the results from other Reynolds numbers in order to see the overall effect of nose radius on leading-edge receptivity.

The results for the $Re = 0$ (flat plate) case are first presented. Figure 12 shows the wall-normal distributions of the amplitude of the streamwise perturbation velocity which were obtained after subtracting the Stokes-wave component. Again the Re_x value for each profile appears at the top.

In the vicinity of the leading edge, we observe that the amplitude profiles develop a shape which we associate with a T-S eigenfunction. These locations are however far upstream of the location of Branch I, so that any T-S modes will decay exponentially with downstream distance until they reach the amplified region.

Starting at the leading edge, we can expect that the velocity fluctuations in the boundary layer are made up of a combination of forced (non-Orr–Sommerfeld) modes, and T-S modes of both discrete and continuous spectrum types. These will grow or decay at different rates so that one may be more dominant than the other at a given streamwise location. For example, in his computational results, Murdock (1981) observed the emergence of oscillations with a wavelength approximately three times the expected T-S wavelength. These occurred further downstream of the leading edge and away from the wall. He associated this with the dominance of T-S-continuous-spectrum modes since their wavelength translated into a phase velocity which was close to the free-stream velocity. With this in mind, we present in figure 13 the amplitude distributions in the streamwise direction at two heights above the surface. These are for $Re = 0$. The two heights are just above the wall at $\eta = 0.033$ (bottom plots), and at the height of the amplitude maximum, $\eta = 1.703$ (top). Figure 13(a) uses an amplitude scale which encompassas the large peak that occurs at the leading edge. Figure 13(b) is a magnified view which is intended to show the oscillations that occur further downstream.

Focusing on the amplitude distributions just above the wall (bottom plots in figure 13a, b), we observe oscillations in the streamwise velocity amplitude which begin right from the leading edge. These quickly decay with downstream distance, however in the magnified view (bottom, figure 13b) we do observe a region of growth. Indicated on Figure 13b are the locations of Branches I and II of the T-S neutral

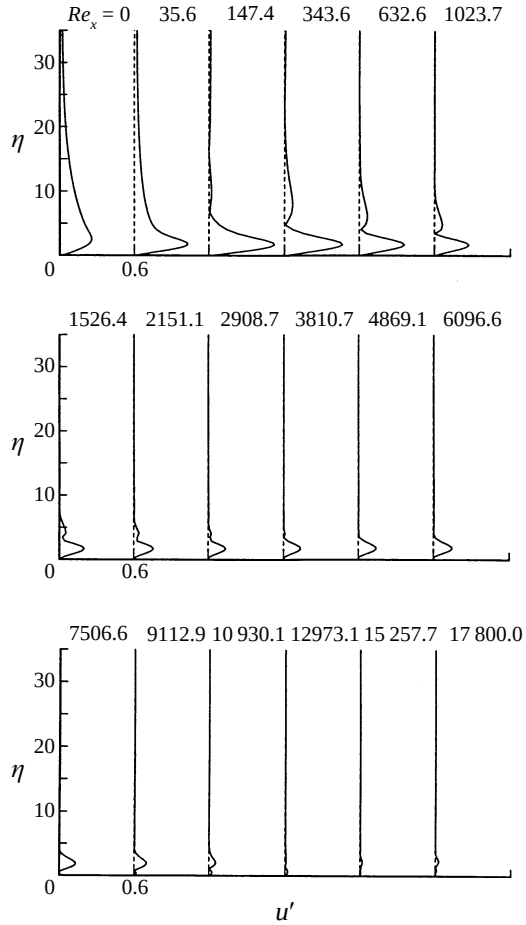

FIGURE 12. Wall-normal profiles of streamwise perturbation velocity amplitude at consecutive downstream locations after subtracting the Stokes wave; $Re = 10$.

growth curve for our free-stream oscillation frequency. The region of growth of the oscillations closely coincides with locations of the neutral branches, which suggests that they are due to T-S waves. The wavelength of the oscillations is fairly constant and compares well with the expected T-S wavelength, where $2\lambda_{TS}$ is indicated on the plot.

The picture looks considerably different when we look at the amplitude fluctuations away from the wall, such as in the upper plots of figure 13. In this case, the magnified views show spatial amplitude oscillations which appear to be modulated, with at least two wavelengths present. Note that this occurs in the downstream region beyond $Re_x = 6000$, where the wall-normal distribution has only a single peak (furthest downstream profiles in figure 12). Murdock (1980) had reasoned that this modulation resulted from the growth of oscillations which were part of the continuous spectrum of the O-S modes. Similar modulations appeared in the numerical solutions by Buter & Reed (1993), by Gatski & Grosch (1987) and in a later computation by Murdock (1981). The amplitude of the modes relevant to the continuous spectrum are larger away from the wall and therefore do not appear in the oscillations just above the wall.

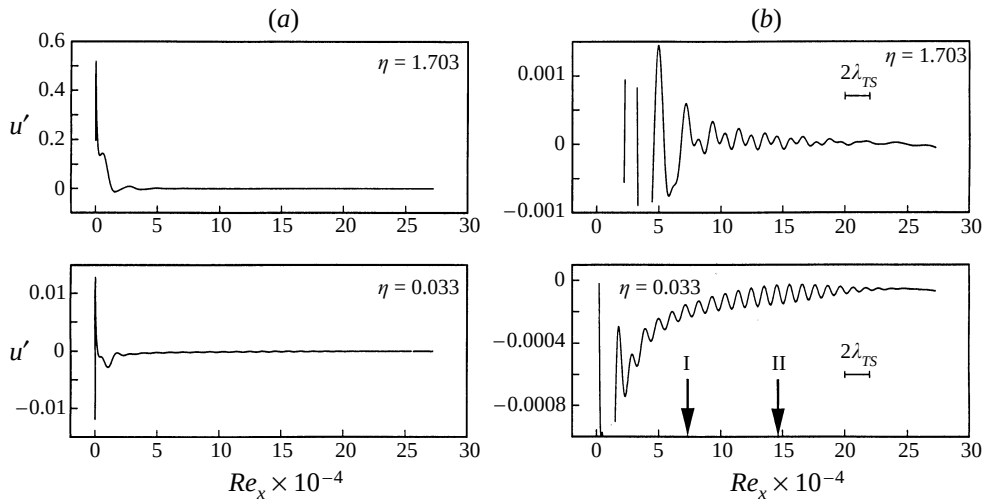

FIGURE 13. (*a*) Amplitude distributions in the streamwise direction at two heights above the surface after subtracting the Stokes wave, with a scale to encompass the peak at leading edge, and (*b*) with a magnified scale to show fluctuations further downstream; $Re = 0$.

The wall-normal distributions of the amplitude of streamwise velocity perturbations for $Re = 10$ are shown in figure 14. These are similar to the $Re = 0$ case in that the profiles have a T-S-eigenfunction shape near the leading-edge. As before, these eventually evolve into a single peak farther downstream. We do observe that the maximum amplitude reached in the profiles is less in this case than with the infinitely sharp leading edge. This is the first evidence of a decrease in the leading edge receptivity with increasing nose radius of curvature.

Amplitude distributions in the streamwise direction for the $Re = 10$ case are shown in figure 15. As with the $Re = 0$ case, these are shown at two heights: just above the wall ($\eta = 3.195$) and where the perturbation amplitude is a maximum ($\eta = 4.865$). Also these are shown with two amplitude scales, one to capture the large peak near the leading edge (figure 15*a*), and the other to view the fluctuations that occur downstream in the T-S amplified region (figure 15*b*). These also show a picture which is comparable to the previous flat-plate case. Namely, near the wall we observe an apparent single-frequency oscillation which initially decays from the leading edge but later amplifies in a range of Re_x which is in the T-S amplification region for our excitation frequency. Again downstream of the leading edge and away from the wall, the amplitude is modulated with two or more wavelengths appearing.

We were interested in showing that a discrete T-S mode was part of the modulated fluctuations that occurred away from the wall. The assumption we made was that the other wavelength mode(s) were part of the continuous spectrum of O-S modes. Since these are expected to have a phase speed approaching the free-stream speed, these would have a wavelength two to three times larger than the discrete T-S wavelength. To remove these, we designed a one-dimensional spatial filter which would reject fluctuations with wavelengths larger than the expected discrete T-S mode. In terms of frequency, this amounts to a one-dimensional, digital, finite impulse response high-pass filter. The impulse response function was designed using a program by McClellan, Parks & Rabiner (1979). The filter cut-off was set to suppress wavelengths which were greater than or equal to twice the expected discrete T-S wavelength. The resulting

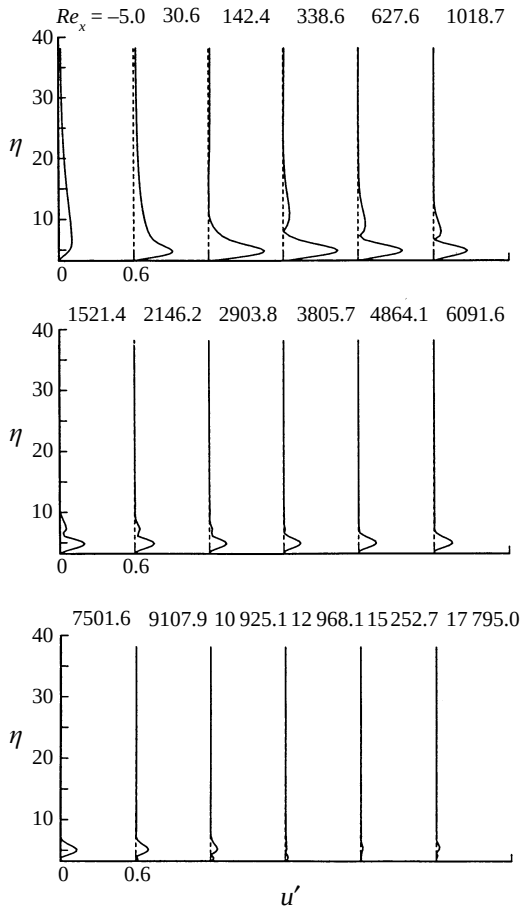

FIGURE 14. Wall-normal profiles of streamwise perturbation velocity amplitude at consecutive downstream locations after subtracting the Stokes wave; $Re = 10$.

response function was convolved with the Stokes-removed u-perturbations in the ξ-direction, for each η in the computational domain. A sample result following filtering is shown in figure 16(a). This shows the amplitude distribution in the streamwise direction at the height of the amplitude maximum. This can be compared to the same amplitude disribution before filtering in the bottom part of figure 15(b).

After filtering we observe a single-frequency oscillation, without amplitude modulation. We also observe two neutral growth locations which coincide well with the theoretical locations of Branches I and II of the T-S neutral curve.

For this same case, we filtered the streamwise amplitude distributions at all the computed heights above the surface of the parabolic body. We measured the maximum amplitude at the x-location of Branch II. These are plotted in the wall-normal (η) direction, and shown as symbols in figure 16(b). For reference we have also plotted as a solid curve the T-S eigenfunction for a linear stability calculation for our excitation frequency and Re_x. The comparison is good and gives evidence that the mode that remains after filtering out the longer wavelength fluctuations is a discrete T-S mode. The slight departure of the computed profile from the linear theory eigenfunction in

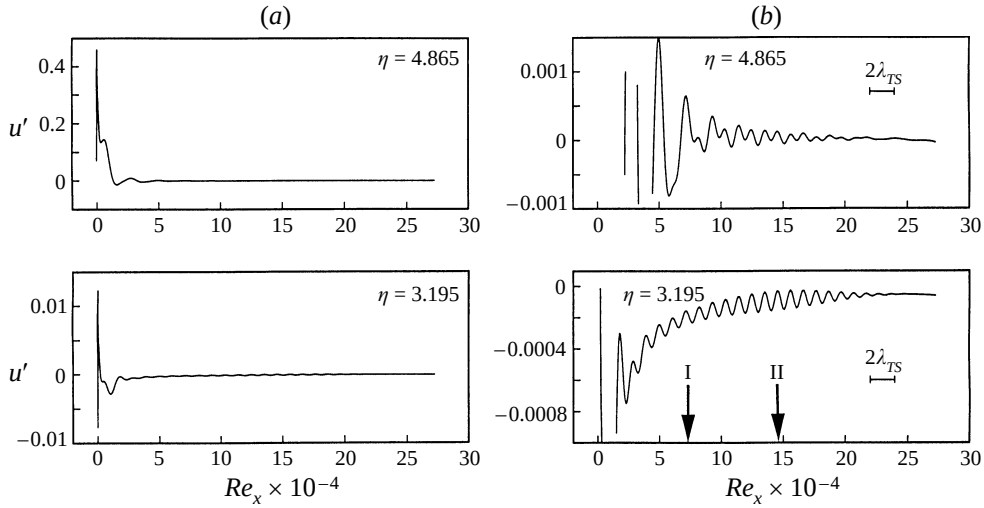

FIGURE 15. (*a*) Amplitude distributions in the streamwise direction at two heights above the surface after subtracting the Stokes wave, with a scale to encompass the peak at leading edge, and (*b*) with a magnified scale to show fluctuations further downstream; $Re = 10$.

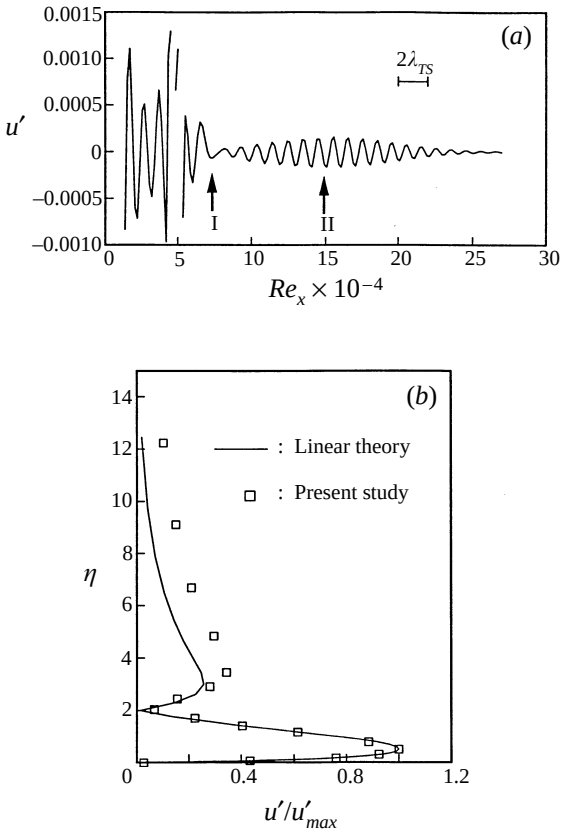

FIGURE 16. (*a*) Amplitude distributions in the streamwise direction at the height of the amplitude maximum, and (*b*) wall-normal profile at the location of Branch II, after filtering long-wavelength fluctuations; $Re = 10$.

the region above the critical layer was also observed in the experiment by Saric *et al.* (1994).

Our final objective is to use the numerical results to determine the value of the leading-edge receptivity and the effect of nose radius of curvature. In determining receptivity, it is necessary to first set a mathematical definition. Surprisingly, in the literature there is no unique definition for receptivity. It can be defined as the ratio of the amplitude of the T-S wave in the boundary layer to the amplitude of the local or free-stream disturbance field. Leehey, Gedney & Her (1984) considered a free-stream disturbance and defined receptivity as the ratio of the maximum amplitude of the T-S-wave response in the boundary layer to that of the free-stream disturbance. Murdock (1980) used the amplitude of the T-S wave at Branch I in his definition of receptivity.

For this study, we define receptivity as the ratio of the maximum T-S amplitude at the leading edge to the amplitude of the free-stream disturbance, i.e. $\mathrm{K}_{LE} = |(u'_{TS})_{LE}|/|(u')_{\infty}|$. One of the advantages of this definition is that an explicit amplitude for the free-stream disturbance is not required. Rather, we only require that the free-stream amplitude be small enough for linearization. By our formulation, the amplitude obtained from the numerical results is u'/u'_{∞}. Therefore, if the only component of fluctuations is due to T-S waves, the amplitude we measure is u'_{TS}/u'_{∞}. Finally, if these are extrapolated back to the leading edge, we have $(u'_{TS})_{LE}/u'_{\infty}$ which is identical to K_{LE}. Therefore the receptivity coefficient can be read directly from the amplitude profiles from which the Stokes wave has been subtracted.

In determining the leading-edge receptivity, we considered two different methods. The first followed the method used by Murdock (1980). It involved fitting an exponential function to the envelope of the absolute value of amplitude fluctuations between the leading edge and the first neutral growth region. This is done in the x-distributions at the height where the amplitude is a maximum, such as in the top part of figure 15(*a*). This method makes no assumption about the origin of the fluctuations, namely if they are forced or O-S modes. The second method attempts to address this. It is based on an exponential extrapolation to the leading edge of the maximum amplitude at streamwise locations where amplitude distributions had a T-S-like eigenfunction shape, for example in the range $140 \leqslant Re_x \leqslant 2000$ shown in figure 12. By this approach, the maximum (lower peak in the T-S eigenfunction) is plotted versus the x-location and used to extrapolate back to the leading edge. A sample of the amplitude distribution based on the second method for $Re = 10$ is shown in figure 17. Shown as the were line is the fit to the points which were used to extrapolate to the leading-edge amplitude.

The two methods were used to determine K_{LE} for different nose Reynolds numbers from 0 to 1250. These are plotted in figure 18. Following Hammerton & Kerschen (1992), we have represented the radius in terms of a Strouhal number, $St = 2\pi f r_n/U_{\infty}$, where f is the physical frequency of the free-stream oscillation. The results show that the leading-edge receptivity coefficient is maximum for the infinitely sharp flat plate, and decreases with increasing nose radius. The difference in the two methods only results in a shift between their respective distributions.

The dependence of the leading-edge receptivity coefficient on nose radius is in good qualitative agreement with the analysis of Hammerton & Kerschen (1992), which shows a decrease in K_{LE} with increasing Strouhal number. We can make a quantitative comparison to the experiment of Saric *et al.* (1994). Their value of the leading-edge receptivity coefficient is shown as the filled square in the left plot of figure 18. This was for a 20 : 1-aspect-ratio super-ellipse matched to a flat plate which was subjected

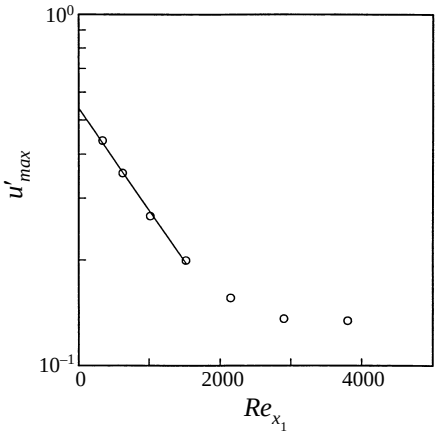

FIGURE 17. Sample streamwise maximum-amplitude envelope used to extrapolate to leading-edge amplitude; $Re = 10$.

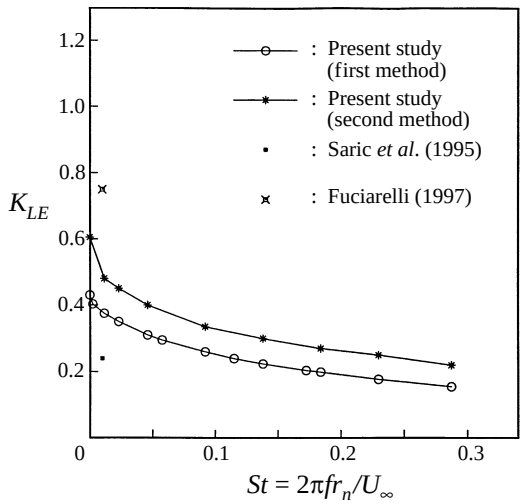

FIGURE 18. Variation of leading-edge receptivity with nose radius.

to a pure-tone free-stream sound source. Although the geometry is different from the parabolic body, this is not a factor in making a comparison to the leading-edge value. As with the computation, the amplitude levels in the experiment are very small which makes the experiments very difficult. As a consequence, the reasonably close values between the experiment and computations is a good confirmation.

We have also included a comparison to the recent numerical results by Fuciarelli (1997). These are for a modified super-ellipse matched to a flat plate for the experimental conditions of Saric *et al.* (1994). Our values are seen to fall between that simulation and the experiment.

6.5. *Effect of angle of attack*

Here we investigated the effect of pressure loading, produced by a mean angle of attack of the parabolic body, on the leading-edge receptivity coefficient. Placing the body at an angle of attack to the free stream results in the movement of the stagnation

point from the body leading edge, and introduces an adverse pressure gradient region on the suction side. As demonstrated in the previous results in § 6.1, at zero angle of attack, the pressure gradient on the parabolic body is everywhere favourable. The effect of a local adverse pressure gradient on the leading-edge receptivity to free-stream sound is our point of interest.

The angle of attack, α, is introduced by a rotational transformation of the coordinate system (x, y) to (x_1, y_1), where

$$x_1 = x\cos\alpha + y\sin\alpha, \tag{39}$$

$$y_1 = y\cos\alpha - x\sin\alpha. \tag{40}$$

The two-dimensional, non-dimensional N-S equations in stream function and vorticity variables, equations (3) and (4), are invariant under this transformation. Changing to parabolic coordinates and introducing the new variables, f and g as before, leads to equations which are identical to (10) and (11), which we later decomposed into the basic and perturbation flows. The only difference that occurs by the transformation involves the free-stream boundary condition on the stream function.

In the free stream, following equation (16), the streamwise velocity component is

$$u_\infty = U_\infty + \tilde{u}_\infty \epsilon\, \mathrm{e}^{\mathrm{i}\sigma t}. \tag{41}$$

Since $u = \partial\psi/\partial y$, with equation (16)

$$U_\infty + \tilde{u}_\infty \epsilon\, \mathrm{e}^{\mathrm{i}\sigma t} = 1 + \epsilon\, \mathrm{e}^{\mathrm{i}\sigma t} \tag{42}$$

from which the free-stream condition is

$$U_\infty = \tilde{u}_\infty = 1. \tag{43}$$

When we incorporate the coordinate rotation, the free-stream condition involving angle of attack in parabolic coordinates is

$$\left[\frac{\xi^2\sin\alpha}{\xi^2+\eta^2} + \frac{\xi\eta\cos\alpha}{\xi^2+\eta^2}\right] f_\xi + \left[\frac{\xi^2\cos\alpha}{\xi^2+\eta^2} - \frac{\xi\eta\sin\alpha}{\xi^2+\eta^2}\right] f_\eta + \left[\frac{\xi\sin\alpha}{\xi^2+\eta^2} + \frac{\eta\cos\alpha}{\xi^2+\eta^2}\right] f = 1. \tag{44}$$

This provides the free-stream boundary condition on f.

The free-stream boundary condition for g is unchanged with angle of attack and therefore identical to equation (15).

We show results for the basic flow for different angles of attack in terms of the wall pressure distribution. These are shown for $Re = 10$ in figure 19. At zero angle of attack, we observe a symmetric distribution about the leading edge. With increasing angle of attack, an asymmetric distribution develops, with a region of adverse pressure gradient occurring on the suction side of the body ($\xi < 0$). As the angle of attack increases, the adverse pressure gradient region moves towards the physical leading edge of the body.

The effect of angle of attack on the leading-edge receptivity is shown in figure 20 for different leading-edge nose radii. The angle of attack is shown on the abscissa and normalized by the square-root of the nose radius (Reynolds number in dimensionless form). This normalization follows Hammerton & Kerschen (1992) except that we used a unit length in place of a wing chord length. In our case to make this dimensionless, we use the nose Reynolds number, Re, and the angle of attack in radians. The ordinate is the leading-edge receptivity coefficient which was determined according to the second method in figure 18. The nose Reynolds numbers and corresponding Strouhal numbers are indicated by the different symbols. In each curve, the frequency

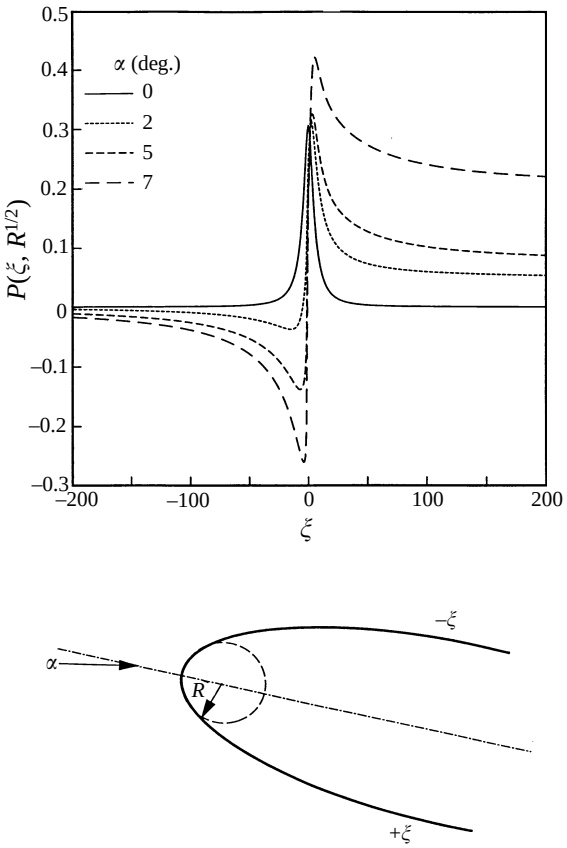

FIGURE 19. Effect of angle of attack on the surface pressure distribution; $Re = 10$.

was kept the same. The different curves correspond to a different nose radius which is indicated by the Reynolds number and Strouhal number. The Strouhal numbers can be used to refer back to figure 18 at zero angle of attack. For each nose radius, we observe an increase in K_{LE} with increasing angle of attack. Here we only considered angles of attack of up to 7°. Over this range, the three sharper leading edges show an approximately 65% increase in the leading-edge receptivity. The physical explanation for this increase, which was suggested by Hammerton & Kerschen (1992), is the movement of the adverse pressure gradient region towards the point of receptivity (leading edge). This can be seen in the pressure distributions ($-\xi$ side) for the $Re = 10$ leading edge in figure 19.

The trend of increasing K_{LE} with angle of attack is consistant with the asymptotic results of Hammerton & Kerschen (1992), although for small aerodynamic loading they observed a slight decrease in the leading-edge receptivity. At larger aerodynamic loading, they observed an increase in the receptivity coefficient. It was with this aspect in mind that we purposely concentrated on smaller angles of attack, and on the same range of Strouhal numbers used by Hammerton & Kerschen. In one case, $St = 0.1$, we observe an initial decrease in K_{LE}; however none of the other Strouhal numbers show this behaviour.

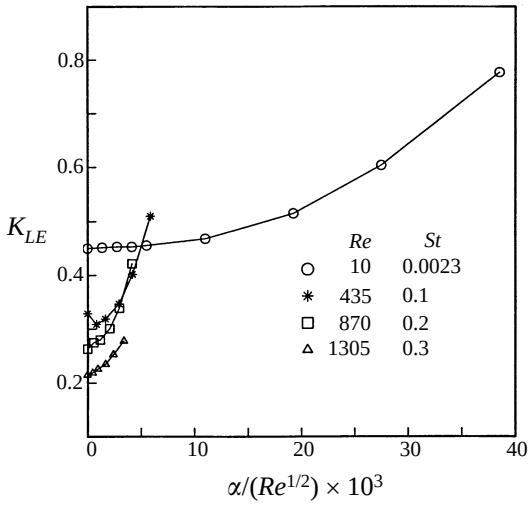

FIGURE 20. Effect of angle of attack on the leading-edge receptivity coefficient for different nose radii.

7. Conclusions

The spatial formulation used in this problem was successful in predicting the evolution of instability waves induced by acoustic free-stream disturbances. We found that the leading-edge receptivity coefficient depended on the nose radius of curvature, with the largest receptivity occurring for the infinitely sharp leading edge. This agreed with the numerical results of Murdock (1980, 1981) and the asymptotic analysis of Hammerton & Kerschen (1992). We also found very good quantitative agreement with the experiment of Saric *et al.* (1994) and the recent numerical results of Fuciarelli (1997). For a given nose radius, the leading-edge receptivity was also found to increase with increased pressure loading produced by a mean angle of attack of the body. This trend agreed with Hammerton & Kerschen (1992) for their larger angles of attack, but did not consistantly show the slight decrease in receptivity that they observed for initial small angles of attack.

The second author is indebted to Professor Thorwald Herbert for introducing this problem to him, and for the support received while on sabbatical leave at Ohio State University and Dynaflow, Inc. The authors have also benefited from discussions on this work with Professors William Saric and Edward Kerschen. Their interest has been greatly appreciated.

REFERENCES

ACKERBERG, R. C. & PHILLIPS, J. H. 1972 The unsteady laminar boundary layer on a semi-infinite flat plate due to small fluctuations in the magnitude of the free-stream velocity. *J. Fluid Mech.* **51**, 137–157.

ANDERSON, D. A., TANNEHILL, J. C. & PLETCHER, R. H. 1984 *Computational Fluid Mechanics and Heat Transfer*. Hemisphere.

BUTER, T. A. & REED, H. L. 1993 Numerical investigation of receptivity to freestream vorticity. *AIAA Paper* 93-0073.

CORKE, T. C. & MANGANO, R. A. 1989 Resonant growth of three-dimensional modes in transitioning Blasius boundary layers. *J. Fluid Mech.* **209**, 93–150.

Davis, R. T. 1972 Numerical solution of the Navier-Stokes equations for symmetric laminar incompressible flow past a parabola. *J. Fluid Mech.* **51**, 417–433.

Fuciarelli, D. 1997 Numerical simulations of leading-edge acoustic receptivity. PhD thesis, Arizona State University.

Gatski, T. B. & Grosch, C. E. 1987 Numerical experiments on boundary-layer receptivity. In *Proc. Symp. on the Stability of Time-Dependent and Spatially Varying Flows*, pp. 82–96. Springer.

Goldstein, M. E. 1983 The evolution of Tollmien-Schlichting waves near a leading edge. *J. Fluid Mech.* **127**, 59–81.

Goldstein, M. E. 1985 Scattering of acoustic waves into Tollmien–Schlichting waves by small streamwise variations in surface geometry. *J. Fluid Mech.* **154**, 509–529.

Haddad, O. M. 1995 Numerical study of leading edge receptivity over parabolic bodies. PhD thesis, Illinois Institute of Technology.

Hammerton, P. W. & Kerschen, E. J. 1992 Effect of nose bluntness on leading-edge receptivity. In *Instability, Transition and Turbulence* (ed. M. Y. Hussaini, A. Kumar & C. L. Streett). Springer.

Herbert, Th. 1991 Numerical study of the leading-edge receptivity. Internal report. Ohio State University, Columbus, Ohio.

Joslin, R. D. & Streett, C. L. 1992 A preliminary study of crossflow transition on a swept wing by spatial direct numerical simulation. In *Instability, Transition and Turbulence* (ed. M. Y. Hussaini, A. Kumar & C. L. Streett). Springer.

Kloker, M., Konzelmann, U. & Fasel, H. 1993 Outflow boundary conditions for spatial Navier-Stokes simulations of transition boundary layers. *AIAA J.* **31**, 620–628.

Leehey, P., Gedney, C. J. & Her, J. Y. 1984 The receptivity of a laminar boundary layer to external disturbances. In *Proc. IUTAM Symp. on Laminar-Turbulent Transition, Novosibrisk, USSR*. (ed. V. V. Kozlov) Springer.

Lin, N. Reed, H. L. & Saric, W. S. 1990 Leading edge receptivity to sound: Navier–Stokes computations. *Appl. Mech. Rev.* **43**, S175.

Lin, N. Reed, H. L. & Saric, W. S. 1992 The effect of leading edge geometry on boundary layer receptivity to freestream sound. In *Instability, Transition and Turbulence* (ed. M. Y. Hussaini, A. Kumar & C. L. Streett), p. 421. Springer.

McClellan, J., Parks, T. & Rabiner, L. 1979 FIR linear phase filter design program. In *Programs for Digital Signal Processing*, IEEE Press, New York.

Murdock, J. W. 1980 The generation of Tollmien–Schlichting wave by a sound wave. *Proc. R. Soc. Lond.* A **372**, 517–534.

Murdock, J. W. 1981 Tollmien–Schlichting waves generated by unsteady flow over parabolic cylindares. *AIAA Paper* 81-0199.

Panton, R. L. 1984 *Incompressible Flow*. John-Wiley.

Saric, W. S. & Rasmussen, B. K. 1992 Boundary layer receptivity: Freestream sound on an elliptical leading edge. *Bull. Am. Phys. Soc.* **37**, 1720.

Saric, W. S., Wei, W. & Rasmussen, B. K. 1994 Effect of leading edge on sound receptivity. In *Laminar-Turbulent Transition, IV, Proc. IUTAM Symp. Sendai, Japan.* (ed. R. Kobayashi).

Shapiro, P. 1977 The influence of sound upon laminar boundary layer instability. *Acoustics and Vibration Lab. Rep.* 83458-83560-1. MIT.

Streett, C. L. & Macaraeg, M. G. 1989 Spectral multi-domain for large-scale fluid dynamics simulations. *Intl J. Appl. Numer. Maths* **6**, 123–140.